coatings

MDPI

Article

Contamination Particle Behavior of Aerosol Deposited Y_2O_3 and YF_3 Coatings under NF_3 Plasma

Je-Boem Song [1,2,†], Eunmi Choi [1,†], Seong-Geun Oh [2], Jin-Tae Kim [1,*] and Ju-Young Yun [1,*]

1 Materials and Energy Measurement Center, Korea Research Institute of Standards and Science (KRISS), Daejeon 34113, Korea; sjb@kriss.re.kr (J.-B.S.); emchoi@kriss.re.kr (E.C.)
2 Department of Chemical Engineering, Hanyang University, Seoul 04763, Korea; seongoh@hanyang.ac.kr
* Correspondence: kimjt@kriss.re.kr (J.-T.K.); jyun@kriss.re.kr (J.-Y.Y.); Tel.: +82-42-868-5624 (J.-Y.Y.)
† These authors contributed equally to this study.

Received: 12 April 2019; Accepted: 5 May 2019; Published: 9 May 2019

Abstract: The internal coatings of chambers exposed to plasma over a long period of time are subject to chemical and physical damage. Contamination particles that are produced by plasma damage to coatings are a major contribution to poor process reliability. In this study, we investigated the behavior of contamination particles produced from plasma damage to Y_2O_3 and YF_3 protective coatings, which were applied by an aerosol deposition method. The coating materials were located at the powered electrode, the grounded electrode, and the grounded wall, which were exposed to a NF_3 plasma. The mass loss at the powered electrode, which was exposed to the NF_3 plasma etching under an applied bias, showed that the YF_3 etching rate was higher than that of Y_2O_3. Conversely, the mass of coating increased at the grounded electrode and the grounded wall, which were exposed to NF_3 plasma etching under zero bias. The mass of the Y_2O_3 coating increased more than that of the YF_3 coating. X-ray photoelectron spectroscopy analysis showed that the Y_2O_3 coating corroded to YO_xF_y in the NF_3 plasma, and YF_3 existed as YF_x. Light scattering sensor analysis showed that the YF_3 coating produced fewer contamination particles than did the Y_2O_3 coating.

Keywords: yttrium oxide (Y_2O_3); yttrium fluoride (YF_3); aerosol deposition (AD); contamination particle; plasma etching; NF_3 plasma

1. Introduction

Efforts to minimize the influence of contamination particles, which are a major cause of decreased production yields, have been continuing as the degree of integration of semiconductor circuits has improved. There are various causes of contamination particles, including mechanical, chemical, and environmental factors. In particular, plasma used in processes for manufacturing semiconductors reacts with parts inside the chamber (e.g., electrodes, showerheads, liners, focusing rings, wall shield rings) to generate contamination particles.

Corroded particles grow on the surface of parts of the inner chamber, which are exposed to plasma ion bombardment and radical reactions over a long period of time. The weakly bonded corrosion particles then fall from the surface as the particles grow in size. As the process repeats, the plasma etches the surface and contamination particles fall off, becoming a major cause of process failure [1]. Corrosion and the extent of etching of parts of the surface are determined by the ion density and ion flux of the exposed plasma. A powered electrode which is exposed to a plasma etching under an applied bias is easily corroded and etched owing to collisions with a large energy flux. The grounded electrode and a grounded wall, which are exposed to a plasma etching under zero bias, sustain limited corrosion and etching by collisions with the ions, which have a low energy flux [2,3]. Ceramic coating films are used to prevent plasma corrosion at these surfaces and minimize the plasma corrosion [4–7].

Among ceramic coating materials for preventing plasma corrosion, Y_2O_3 is widely used for inner parts of the chamber because of its low etching rate and low chemical reactivity. Recently, YOF and YF_3 have also drawn attention as ceramic coating materials for parts owing to their ability to suppress chemical reactions with fluoridated gases such as CF_4 and NF_3 [8–13]. Nevertheless, there have been few reports about the behavior of contamination particles by plasma etching [14]. Atmospheric plasma spraying (APS) methods are commonly used to coat parts with ceramic coating materials such as Y_2O_3 and YF_3. The APS method melts a ceramic powder, with particles sizes in the range of several tens of micrometers, in a high-temperature plasma (10,000 K or more), which attaches to the substrate. The APS method enables the coating of thick films in a short period of time, but provides a rough surface and layered structure, such that the adhesion with the surface is poor and the coating peels off easily. Furthermore, such coatings have a low density owing to numerous internal pores [15]. The aerosol deposition (AD) method has been studied as a coating technology to overcome the limitations of APS. The AD method involves spraying a sub-micrometer-sized powder with high-pressure air through a nozzle in a vacuum chamber ($>10^{-3}$ Torr). The AD method coats a high-density film with excellent uniformity of thickness compared with that of the APS method [16–19]. The plasma etching properties of ceramic coatings coated by the APS method have been reported in previous studies [8]; however, there is a lack of studies on the properties of ceramic coatings prepared by AD methods, including plasma etching properties and the generation of contamination particles. The etching properties of CF_4 gas, which is used in the etching process, have been widely studied. However, etching with CF_4 gas is often accompanied by the formation of unwanted fluorocarbon polymer layers. Recently, completely dissociated NF_3 has been used to minimize these unwanted reactions and to achieve high etch rates [20–23].

In this study, we discuss the etching properties and contamination particles generation of Y_2O_3 and YF_3 coatings fabricated by the AD method utilizing the NF_3 plasma process. We investigated locations including the powered electrode, grounded electrode, and grounded wall to observe the etching characteristics of the coating material and the dependence on the bias voltage.

2. Materials and Methods

Figure 1 shows a schematic diagram of the capacitively coupled plasma system. The dimensions of the reactor were an inner diameter of 30 cm and a height of 30 cm. The powered electrode and grounded electrode had a radius of 7.6 cm. The discharge gap length from the powered electrode to the grounded electrode was 10 cm. Specimens were placed in the powered electrode, grounded electrode, and grounded wall, as shown in Figure 1.

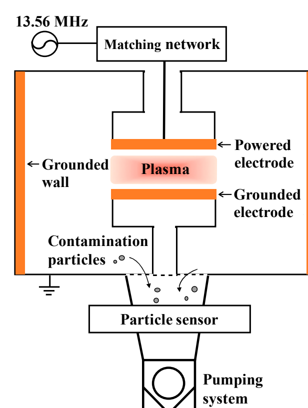

Figure 1. Schematic diagram of the capacitively coupled plasma etching system. A specimen was placed in the powered electrode, grounded electrode, and grounded wall.

The NF_3 gas was used to generate a plasma supplied through a showerhead with a mass flow controller. A dry pump and turbo pump were used in the vacuum system, and the working pressure of the experiment was 40 Pa. The power was set to be 13.56 MHz (Sizer Generator, Advanced Energy, Fort Collins, CO, USA), and an impedance matching network (Navigator, Advanced Energy, Fort Collins, CO, USA) was used to deliver the maximum power. The RF power applied to the plasma was 400 W. During the plasma etching, the temperatures at the powered electrode, grounded electrode, and grounded wall were about 120, 60, and 50 °C, respectively. The temperature was measured using an IR thermometer (IMPAC Pyrometer IN5, Lumasense Technologies, Santa Clara, CA, USA) and the temperature inside the chamber was measured through a viewport with zinc selenide.

The disc-like substrates were made of Al alloy 6061 and had a diameter of 76 mm and thickness of 1 mm. The substrates were then coated with Y_2O_3 and YF_3 by AD, with the use of an aerosol deposition system (Dandan Corp., Daejeon, Korea), where Y_2O_3 and YF_3 were in a powder form (99.99%, D50 = 0.5–5 μm). The sprayed coatings of Y_2O_3 and YF_3 were 8 and 19 μm thick, respectively. The AD coating was performed as follows: the air flow rates were 40–80 SLM and the vacuum pressure was 10 Pa.

Before and after the NF_3 plasma etching, the surface morphology and composition of the Y_2O_3 and YF_3 coatings were ex-situ analyzed with a field-emission scanning electron microscope (FE-SEM, S-4800, Hitachi, Tokyo, Japan) and X-ray photoelectron spectroscopy (XPS; Monochromatic Al-Kα, AXIS-NOVA, Manchester, UK), respectively. The mass of the specimen was measured before and after the plasma etching test with a XP205 analytical balance (Mettler Toledo, Greifensee, Switzerland). After the plasma etching was performed for 60 min, the specimen was removed, and the mass loss was measured. The contamination particles produced from the Y_2O_3 and YF_3 coatings were measured in real time according to the NF_3 plasma exposure time. An ISPM light-scattering sensor (Stiletto, In Situ Particle Monitor, Inficon, Heidiland, Switzerland) was attached to the exhaust line to measure the amount and size of the contamination particles. This system was capable of measuring contamination particles in real time as they passed through the exhaust pipe. The ISPM was placed in the exhaust line so that it detected particles moving in one direction. The ISPM does not operate properly when exposed to the light of the plasma, because of excess noise. The minimum measurable particle size was ~0.2 μm. The sensor was based on the principles of laser light scattering, and more details of its working principles can be found in previous reports [24,25].

3. Results and Discussion

Figure 2 shows an FE-SEM image of Y_2O_3 and YF_3 powders used as a starting material for coating. The Y_2O_3 powder (Figure 2a,b) and YF_3 powder (Figure 2c,d) were composed of flat particles approximately 1–5 μm in size, and spherical particles approximately 0.5–1 μm in size, respectively. Furthermore, the YF_3 powder showed greater aggregation than that of the Y_2O_3 powder. We expected that the YF_3 powder was sprayed as a mixed powder, containing dispersed particles in the size range of 0.5–1 μm together with aggregated particles larger than 1 μm, because aggregated particles are not easily dispersed. When we applied the AD method, the Y_2O_3 and YF_3 particles were sprayed by pressurized gas. The accelerated particles had a kinetic energy, which dissipated on collision with the substrate [17]. In this case, plastic deformation or fracturing of particles might occur owing to the high kinetic energy of large sprayed particles [18]. Particles tend to fracture when they aggregate or have a high kinetic energy owing to their large size, as shown in Figure 3.

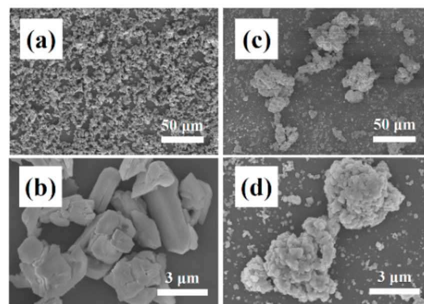

Figure 2. FE-SEM images of Y_2O_3 and YF_3 powders before coating by aerosol deposition: (**a**,**b**) Y_2O_3 powder and (**c**,**d**) YF_3 powder.

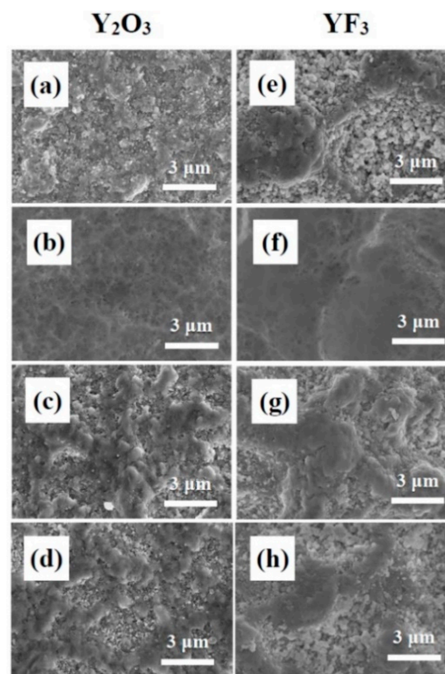

Figure 3. FE-SEM images of the surface of Y_2O_3 and YF_3 coatings before and after exposure to NF_3 plasma: (**a**) Y_2O_3 and (**e**) YF_3 before etching; (**b**) Y_2O_3 and (**f**) YF_3 after etching of the powered electrode; (**c**) Y_2O_3 and (**g**) YF_3 after etching of the grounded electrode; (**d**) Y_2O_3 and (**h**) YF_3 after etching of the grounded wall.

The Y_2O_3 powder consisted of particles approximately 1–5 μm in size (Figure 2), and the Y_2O_3 particles were coated mainly by plastic deformation; however, fragmentation of larger particles into smaller particles was caused by their high kinetic energies at the moment of collision with the substrate. In this case, a film failed to form or only a residue formed (Figure 3a). The average particle size was 0.5–1 μm, but most aggregated YF_3 particles were separated when they collided with the substrate, and formed a porous film. For this reason, before the NF_3 plasma etching, the initial YF_3 coating film (Figure 3e) and the Y_2O_3 coating film (Figure 3a) showed different surface properties. However, the final coating was denser than the initial coating film, because the initial coating was subjected to particles with high kinetic energy, which had a hammering effect. After the NF_3 plasma etching, we confirmed that the coating surface changed depending on the position in the chamber. The Y_2O_3 (Figure 3b) and YF_3 (Figure 3f) coatings on the powered electrode were rapidly corroded and etched. The NF_3 plasma etching under an applied bias removed the initial surface and exposed a uniform surface, which was subjected to the hammering effect. Conversely, the Y_2O_3 (Figure 3c,d) and YF_3 (Figure 3g,h) coatings at the grounded electrode and the grounded wall appeared to mix with the surface and took on a rough morphology similar to that of the powered electrode surface.

We attribute these surface properties to two factors. First, the surface was hardly corroded or etched by the NF_3 plasma etching under zero bias. Rather, some by-products (contamination particles) were deposited, such as YO_xF_y or YF_x, which were generated from etching of the powered electrode by NF_3. As evidence for this change, we considered the mass change after exposure to the NF_3 plasma (Figure 4). After exposure to NF_3, the masses of the Y_2O_3 and YF_3 coatings located on the powered electrode decreased (Figure 4a). The masses of the Y_2O_3 and YF_3 coatings located on the grounded electrode and the grounded wall increased (Figure 4b,c).

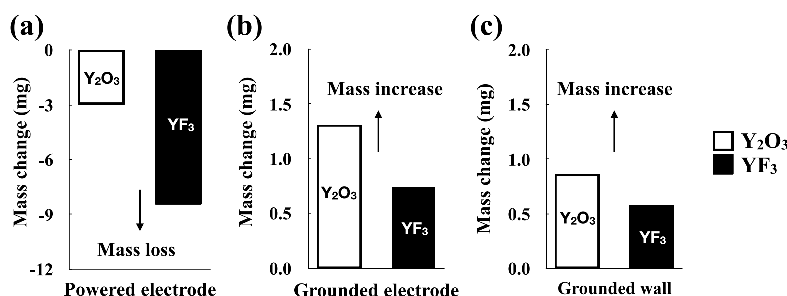

Figure 4. Mass changes owing to the NF_3 plasma etching: Y_2O_3 and YF_3 coatings. (**a**) Y_2O_3 and YF_3 after etching of the powered electrode; (**b**) Y_2O_3 and YF_3 after etching of the grounded electrode; (**c**) Y_2O_3 and YF_3 after etching of the grounded wall.

Next, the surfaces of the coating located on the grounded electrode and the grounded wall were maintained in the same state as before exposure to the NF_3 plasma. The plasma density was highest at the center of the chamber and lower at the edges [26]. The grounded electrode and grounded wall were exposed to NF_3 plasma etching under zero bias. Thus, the etching reaction occurred very slowly, and even after exposure to NF_3 plasma, the Y_2O_3 coating on the grounded electrode and grounded wall contained very small particles generated by the fracturing of larger particles (Figure 3c,d), and the YF_3 coating had a porous structure composed of fractured and aggregated particles (Figure 3g,h).

Finally, the coating of the grounded electrode showed a greater mass change than that of the grounded wall coating. If sputtering of by-products occurs, the grounded electrode will be more affected than the grounded wall because it is located directly below the powered electrode. Figure 4b,c shows that both the Y_2O_3 and YF_3 coatings had a considerably greater mass increase for the grounded electrode compared with that for the grounded wall coating. In addition, the initial surface of the grounded wall (Figure 3d,h) showed better resistance than that of the grounded electrode (Figure 3c,g) for both the Y_2O_3 and YF_3 coatings.

Compared with Y_2O_3, the YF_3 coatings were more rapidly etched and showed greater mass loss under the NF_3 plasma (Figure 4a). The standard boiling temperatures defined by IUPAC of Y_2O_3 and YF_3 are 4570 and 2500 K, respectively, and the sublimation enthalpy of Y_2O_3 is also greater than that of YF_3. Thus, Y_2O_3 forms stronger bonds than does YF_3 [8]. Therefore, for an etching reaction occurring under the same conditions, YF_3 is etched more rapidly than is Y_2O_3. We estimated the etching rates of the Y_2O_3 and YF_3 coatings on the powered electrode from mass loss to be 48 and 186 nm/min/m^2, respectively.

Notably, although the mass of the YF_3 coating located on the powered electrode decreased considerably compared with that of the Y_2O_3 coating, the mass increases of the YF_3 coatings located on the grounded electrode and the grounded electrode were less than those of the Y_2O_3 coating. This result is difficult to explain if simply considering the sputtering of by-products. We posit that fluorine deposition occurs in addition to the sputtering of by-products. Schaepkens et al. reported that fluorine gas takes precedence over etching where a self-bias voltage is present, and deposition occurred where the self-bias voltage was absent [27]. On this basis, we speculate that fluorine deposition occurred on the grounded electrode and grounded wall where the self-bias voltage was absent. In particular, the Y_2O_3 coating was more greatly affected by fluorine deposition than the YF_3 coating because of the

many oxygen atoms and vacancies that can react with fluorine. As a result, by-product sputtering and fluorine deposition occurred at the same time in the coating of the grounded wall and grounded electrode during exposure to NF_3 plasma. The Y_2O_3 coating mass greatly increased because the Y_2O_3 coating was affected more by the fluorine deposition reaction than was the YF_3 coating. On the other hand, the YF_3 coating was affected more by the sputtering of by-product reaction than the fluorine deposition reaction.

We had previously confirmed that the Y_2O_3 coating reacts with NF_3 plasma to form YO_xF_y, which is etched by ion attack, and the YO_xF_y coating is etched in the form of YO_xF_y without a principal chemical reaction [8]. On the basis of previous studies, the YF_3 coating is also expected to be etched in the form of YF_x without notable chemical corrosion reactions (Figure 5). We measured the amounts of Y, O, and F in the Y_2O_3 and YF_3 coatings by XPS analysis after exposure to NF_3 plasma to confirm the etching mechanism (Table 1). The YF_3 coating showed no notable component changes before and after exposure to NF_3 plasma. However, the Y_2O_3 coating had a lower O 1*s* content and a greater F 1*s* content.

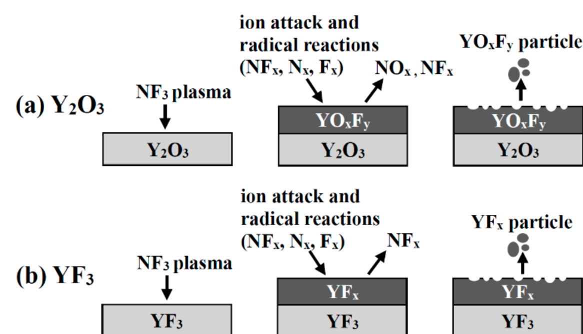

Figure 5. Schematic diagram of yttrium oxyfluoride film deposition and etching behavior of (**a**) Y_2O_3 and (**b**) YF_3 coatings.

Table 1. X-ray photoelectron spectroscopy (XPS) analysis results of Y_2O_3 and YF_3 coatings before and after exposure to NF_3 plasma: (**a**) Y_2O_3 and (**e**) YF_3 before etching; (**b**) Y_2O_3 and (**f**) YF_3 after etching of the powered electrode; (**c**) Y_2O_3 and (**g**) YF_3 after etching of the grounded electrode; (**d**) Y_2O_3 and (**h**) YF_3 after etching of the grounded wall.

Compound Content (at.%)	Y_2O_3 Coating				YF_3 Coating			
	(a)	(b)	(c)	(d)	(e)	(f)	(g)	(h)
Y 3*d*	31.8	29.2	27.3	25.4	33.7	30.1	28.7	29.0
O 1*s*	65.1	13.0	11.6	14.2	5.7	3.1	2.9	3.0
F 1*s*	3.1	57.8	61.1	60.4	60.6	66.8	68.4	68.0

Figure 6 shows the XPS spectra of yttrium in Y_2O_3 and YF_3 before and after the NF_3 plasma treatment for more precise analysis. We designated the XPS peaks for the cations of Y $3d_{5/2}$ and Y $3d_{3/2}$ as blue, green, and orange lines, respectively. The binding energy difference of the two peaks was 2.05 eV, which represents an intensity ratio of 3:2. The Y $3d_{5/2}$ and Y $3d_{3/2}$ spectra were fitted by a ratio of 10:90 (Gaussian/Lorentzian). In the case of Y_2O_3 before the reaction with NF_3 plasma, the Y $3d_{5/2}$ peak positions (green line) were 157.8 and 156.2 eV, and the Y $3d_{3/2}$ peak positions (orange line) were 160.1 and 158.3 eV. However, after the reaction with the NF_3 plasma, the binding energy of Y $3d_{5/2}$ (blue line) and Y $3d_{3/2}$ shifted to 159 and 161.5 eV, respectively; hence, Y–F bonds formed.

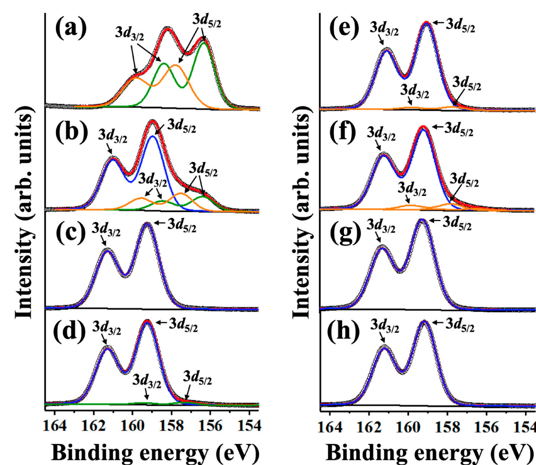

Figure 6. X-ray photoelectron spectroscopy (XPS) results: (**a**) Y_2O_3 and (**e**) YF_3 before etching, (**b**) Y_2O_3 and (**f**) YF_3 after etching of the powered electrode; (**c**) Y_2O_3 and (**g**) YF_3 after etching of the grounded electrode; (**d**) Y_2O_3 and (**h**) YF_3 after etching of the grounded wall.

Figure 6a shows the three Y–O peaks located at 159.9, 158.1, and 156.2 eV (red line). As shown in Figure 6b–d, the peak position shifted to higher binding energy after the reaction with the NF_3 plasma. Because the F ion has a very high electron affinity, the binding length with the cation X was shortened, the electron density was decreased, and the binding energy increased when the X–O bond was substituted with the X–F bond [7]. After the reaction with the NF_3 plasma, the Y–O bonds were substituted with Y–F bonds, and the binding energy increased owing to the difference in electronegativity between the two bonds. This result confirms that the Y_2O_3 coating of the powered electrode featured coexisting Y–O and Y–F bonds because the surface of Y_2O_3 coating was etched. At the grounded electrode and the grounded wall, the Y–O bonds on the surface were completely substituted by Y–F owing to the high reactivity of fluorine radicals; hence, the surface had an apparent binding energy peak similar to that of YF_3. Conversely, as shown in Figure 6e–h, the YF_3 coating exhibited less change in its composition before and after NF_3 plasma treatment. As a result, we confirmed that the previously expected mechanisms for the reaction of the NF_3 plasma with Y_2O_3 and YF_3 coatings were reasonable.

Finally, we measured the contamination particles generated in real time in the NF_3 plasma environment for 60 min in order to confirm the formation behavior of contaminating particles from the Y_2O_3 and YF_3 coatings (Figure 7). Figure 7 shows the concentration and the cumulative concentration of contamination particles generated in real time. During the initial 10 min, contaminating particles were rarely generated at the Y_2O_3 and YF_3 coating films. This is thought to be due to the growth mechanism of the contamination particles and the surface temperature change of the powered electrode by plasma applied bias. The contamination particles initially grow on the coating surface, and the grown contamination particles are dropped off at the weakened bond sites. Also, the surface temperature of the powered electrode was increased to 120 °C while being heated by plasma applied bias, and then maintained at 120 °C by cooling systems. When the coating material reached 120 °C, the coating films became stressed because of the difference in the thermal expansion coefficient between the aluminum used as the base material and the coating material, and grown contamination particles more easily fell off from the surface. Hence, during the initial 10 min, contaminating particles were rarely generated because it takes time to grow contamination particles and raise the temperature of the powered electrode. The results show that more contamination particles were generated in the Y_2O_3 coating. This finding contradicts the results of mass loss measurements by etching of the YF_3 and Y_2O_3 coatings, as discussed previously. As mentioned above, Y_2O_3 reacted with the NF_3 plasma to produce YO_xF_y, a volatile gas, and NO_x. The YF_3 produced YF_x and NF_x gas without any notable chemical changes (Figure 5). Hence, the chemical corrosion of the Y_2O_3 coating was faster when subjected to

NF_3 plasma than was the YF_3 coating, which means that the contamination particles grew faster on the Y_2O_3 coating surface than on the YF_3 coating. However, Y_2O_3 has a higher binding energy than that of YF_3; hence, the growth of contamination particles from the Y_2O_3 coating was slower than for the YF_3 coating.

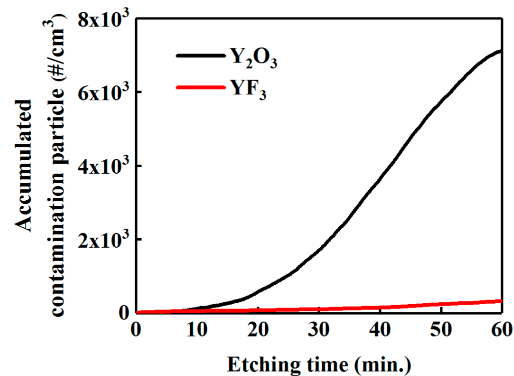

Figure 7. Real-time detection of accumulated contamination particle concentration, over 0.2 μm size, generated from Y_2O_3 and YF_3 during the 60 min NF_3 plasma treatment.

As a result, YF_3 is stable to chemical corrosion when subject to the NF_3 plasma; however, the weak physical binding force resulted in rapid etching and produced fewer contamination particles of a critical size, which could act as defects in the actual plasma process. The Y_2O_3 was slowly etched because of the strong physical binding forces, but was susceptible to chemical corrosion by the NF_3 plasma, which caused large contamination particles, which act as defects in the actual plasma process [18,22].

4. Conclusions

We prepared Y_2O_3 and YF_3 coatings by AD and subjected these to NF_3 plasma. Owing to the characteristics of the starting materials, the initial surfaces had different properties. However, the Y_2O_3 and YF_3 coatings placed at the powered electrode were rapidly etched by the NF_3 plasma treatment. Less etching occurred at the grounded electrode and the grounded walls, and the mass at these surfaces increased owing to sputtering of by-products and fluorine deposition. Additionally, the Y_2O_3 coating showed more rapid chemical corrosion than did the YF_3 coating, and many contamination particles were generated, which acted as defects. This study demonstrates that the YF_3 coating has the potential to be used as a candidate material to reduce contaminating particles in the semiconductor etching process.

Author Contributions: Conceptualization, J.-B.S. and E.C.; Methodology, J.-B.S.; Investigation, J.-B.S. and E.C.; Writing—Original Draft Preparation, J.-B.S. and E.C.; Writing—Review and Editing, J.-B.S., E.C., J.-T.K., S.-G.O., and J.-Y.Y.; Supervision, J.-T.K., S.-G.O., and J.-Y.Y.

Funding: This research was funded by the R&D Convergence Program of National Research Council of Science and Technology (NST) of the Republic of Korea (NST, CAP-16-04-KRISS) and Development of Fundamental Technology for Industrial Metrology funded by Korea Research Institute of Standards and Science (KRISS-2019-GP2019-0011).

Acknowledgments: We would like to Kang-Ho Lee and Jung-Nam Park of Dandan Corporation for providing aerosol-deposited Y_2O_3 and YF_3 coatings. We are thankful to our colleagues Seung-Su Lee, Minjoong Kim, and Jong-Ho So, who assisted with some experiments.

Conflicts of Interest: The authors declare no conflict of interest.

References

1. Kasashima, Y.; Nabeoka, N.; Motomura, T.; Uesugi, F. Many flaked particles caused by impulsive force of electric field stress and effect of electrostriction stress in mass-production plasma etching equipment. *Jpn. J. Appl. Phys.* **2014**, *53*, 040301. [CrossRef]
2. Chu, P.K.; Qin, S.; Chan, C.; Cheung, N.W.; Ko, P.K. Instrumental and process considerations for the fabrication of silicon-on-insulators (SOI) structures by plasma immersion ion implantation. *IEEE Trans. Plasma Sci.* **1998**, *26*, 79–84. [CrossRef]
3. Yang, Y.; Kushner, M.J. Modeling of dual frequency capacitively coupled plasma sources utilizing a full-wave Maxwell solver: II. Scaling with pressure, power and electronegativity. *Plasma Sources Sci. Technol.* **2010**, *19*, 055012. [CrossRef]
4. Shin, J.S.; Kim, M.; Song, J.B.; Jeong, N.G.; Kim, J.T.; Yun, J.Y. Fluorine plasma corrosion resistance of anodic oxide film depending on electrolyte temperature. *Appl. Sci. Converg. Technol.* **2018**, *27*, 9–13. [CrossRef]
5. Song, J.B.; Kim, J.T.; Oh, S.G.; Shin, J.S.; Chun, J.R.; Yun, J.Y. Effect of sealing time of anodic aluminum oxide (AAO) film for preventing plasma damage. *Sci. Adv. Mater.* **2015**, *7*, 127–132. [CrossRef]
6. Cao, Y.C.; Zhao, L.; Luo, J.; Wang, K.; Zhang, B.P.; Tokota, H.; Ito, Y.; Li, J.F. Plasma etching behavior of Y_2O_3 ceramics: Comparative study with Al_2O_3. *Appl. Surf. Sci.* **2016**, *366*, 304–309. [CrossRef]
7. Kim, D.M.; Lee, S.H.; Alexander, W.B.; Kim, K.B.; Oh, Y.S.; Lee, S.M. X-ray photoelectron spectroscopy study on the interaction of yttrium-aluminum oxide with fluorine-based plasma. *J. Am. Ceram. Soc.* **2011**, *94*, 3455–3459. [CrossRef]
8. Tahara, R.; Tsunoura, T.; Yoshida, K.; Yano, T.; Kishi, Y. Fabrication of dense yttrium oxyfluoride ceramics by hot pressing and their mechanical, thermal, and electrical properties. *Jpn. J. Appl. Phys.* **2018**, *57*, 06JF04. [CrossRef]
9. Lin, T.K.; Wuu, D.S.; Huang, S.Y.; Wang, W.K. Preparation and characterization of sprayed-yttrium oxyfluoride corrosion protective coating for plasma process chambers. *Coatings* **2018**, *8*, 373. [CrossRef]
10. Wang, W.K.; Lin, Y.X.; Xu, Y.J. Structural and fluorine plasma etching behavior of sputter-deposition yttrium fluoride film. *Nanomaterials* **2018**, *8*, 936. [CrossRef]
11. Ma, T.; List, T.; Donnelly, V.M. Comparisons of NF_3 plasma-cleaned Y_2O_3, YOF, and YF_3 chamber coatings during silicon etching in Cl_2 plasmas. *J. Vac. Sci. Technol. A Vac. Surf. Films* **2018**, *36*, 0734. [CrossRef]
12. Shiba, Y.; Teramoto, A.; Goto, T.; Kishi, Y.; Shirai, Y.; Sugawa, S. Stable yttrium oxyfluoride used in plasma process chamber. *J. Vac. Sci. Technol. A Vac. Surf. Films* **2017**, *35*, 021405. [CrossRef]
13. Kim, D.M.; Jang, M.R.; Oh, Y.S.; Kim, S.; Lee, S.M.; Lee, S.H. Relative sputtering rates of oxides and fluorides of aluminum and yttrium. *Surf. Coat. Technol.* **2017**, *309*, 694–697. [CrossRef]
14. Song, J.B.; Kim, J.T.; Oh, S.G.; Yun, J.Y. Contamination particles and plasma etching behavior of atmospheric plasma sprayed Y_2O_3 and YF_3 coatings under NF_3 plasma. *Coatings* **2019**, *9*, 102. [CrossRef]
15. Pawlowski, L. *The Science and Engineering of Thermal Spray Coatings*, 2nd ed.; John Wiley & Sons: Chichester, UK, 2008.
16. Fan, W.; Bai, Y. Review of suspension and solution precursor plasma sprayed thermal barrier coatings. *Ceram. Int.* **2016**, *42*, 14299–14312. [CrossRef]
17. Hanft, D.; Exner, J.; Schubert, M.; Stöcker, T.; Fuierer, P.; Moos, R. An overview of the aerosol deposition method: Process fundamentals and new trends in materials applications. *J. Ceram. Sci. Technol.* **2015**, *6*, 147–182. [CrossRef]
18. Akedo, J. Aerosol deposition of ceramic thick films at room temperature: Densification mechanism of ceramic layers. *J. Am. Ceram. Soc.* **2006**, *89*, 1834–1839. [CrossRef]
19. Choi, H.; Kim, K.; Choi, H.; Kang, S.; Yun, J.; Shin, Y.; Kim, T. Plasma resistant aluminum oxide coatings for semiconductor processing apparatus by atmospheric aerosol spray method. *Surf. Coat. Technol.* **2010**, *205*, S125–S128. [CrossRef]
20. Machima, P.; Hershkowitz, N. SiO_2 and Si_3N_4 etch mechanisms in NF_3/hydrocarbon plasma. *J. Phys. D Appl. Phys.* **2006**, *39*, 673. [CrossRef]
21. Ji, B.; Yang, J.H.; Badowski, P.R.; Karwacki, E.J. Optimization and analysis of NF_3 in situ chamber cleaning plasmas. *J. Appl. Phys.* **2004**, *95*, 4452–4462. [CrossRef]

22. Kastenmeir, B.E.E.; Matsuo, P.J.; Oehrlein, G.S.; Langan, J.G. Remote plasma etching of silicon nitride and silicon dioxide using NF_3/O_2 gas mixtures. *J. Vac. Sci. Technol. A Vas. Surf. Films* **1998**, *16*, 2047–2056. [CrossRef]
23. Matsuo, P.J.; Kastenmeier, B.E.E.; Oehrlein, G.S.; Langan, J.G. Silicon etching in NF_3/O_2 remote microwave plasmas. *J. Vac. Sci. Technol. A Vas. Surf. Films* **1999**, *17*, 2431–2434. [CrossRef]
24. Miyashita, H.; Kikuchi, T.; Kawasaki, Y.; Katakura, Y.; Ohsako, N. Particle measurements in vacuum tools by in situ particle monitor. *J. Vac. Sci. Technol. A Vac. Surf. Films* **1999**, *17*, 1066–1070. [CrossRef]
25. Hulst, H.C. *Light Scattering by Small Particles*; Dover Publications, Inc.: New York, NY, USA, 1981.
26. Lee, H.C.; Bang, J.Y.; Chung, C.W. Effects of RF bias power on electron energy distribution function and plasma uniformity in inductively coupled argon plasma. *Thin Solid Films* **2011**, *519*, 7009–7013. [CrossRef]
27. Schaepkens, M.; Oehrlein, G.S. A review of SiO_2 etching studies in inductively coupled fluorocarbon plasmas. *J. Electrochem. Soc.* **2001**, *148*, C211–C221. [CrossRef]

© 2019 by the authors. Licensee MDPI, Basel, Switzerland. This article is an open access article distributed under the terms and conditions of the Creative Commons Attribution (CC BY) license (http://creativecommons.org/licenses/by/4.0/).